A New and Practical Formulation of Bistatic Inverse Synthetic Aperture Radar Imaging and Verification of the Formulation using Numerical Examples

Caner Ozdemir[1], Sevket Demirci[1], Betul Yilmaz[1], Cevher Ak[1] and Enes Yigit[2]

[1]Mersin University, Dept. of Electrical-Electronics Engineering Mersin University Ciftlikkoy 33343, Mersin, Turkey
cozdemir@mersin.edu.tr, sdemirci@mersin.edu.tr, betuly@mersin.edu.tr, cevher.ak@mersin.edu.tr
[2]Mersin University, Vocational School of Technical Sciences, Ciftlikkoy 33343, Mersin, Turkey
enesyigit81@mersin.edu.tr

Abstract

A compact formulation of bistatic Inverse Synthetic Aperture Radar (ISAR) imaging is provided and presented thru numerical simulation of various perfect scatterers. The imaging formulation is derived for small-angle and small-bandwidth conventions. After completing the formulation, its relationship to monostatic set-up is examined and discussed. To validate the algorithm, the images of point target models are then simulated and presented for different bistatic geometries. It is shown that for a range of bistatic angle, the imaging algorithm successfully works and has the advantage of reduced bandwidth over the monostatic case at the cost of worse resolution.

1. Introduction

ISAR image of a target plays an important role in military applications such as target identification, recognition and classification [1]. In these applications, demanding requirement on the image is to achieve sharp resolutions in both down-range and cross-range domains [2]. For Synthetic Aperture Radar (SAR) and ISAR scenarios, the down-range resolution is achieved by varying the frequency of the transmitted pulse. Therefore, there always exists a trade-off between the range resolution and the frequency bandwidth. In contrary to SAR, the radar is fixed in the ISAR problem and the cross-range resolution is attained by target's motion that is generally unknown to the radar engineer. In order to successfully form a radar image, the target's illumination angle has to be altered with respect to radar. But in some instances, especially when the target is moving along the radar Line Of Sight (LOS), the viewing angle cannot be sufficient to be able form an ISAR image [2]. To overcome this restriction, the application of bistatic ISAR geometries that provide adequate look-angle diversity of the target has been taken into consideration in recent studies [3-5]. In this work, we have reviewed and reorganized these studies to obtain a concise and computationally fast algorithm for bistatic ISAR imaging.

Previously, we have formulated and successfully formed the ISAR images of large and complex targets for the monostatic configuration [6-7]. In this paper, the problem is extended and related to the bistatic case by deriving the imaging equation under the small-angle and small-bandwidth assumptions. The derivation is then applied over numerical simulations for targets of perfect point scatterers. In the next section, the geometry of the problem is illustrated and theoretical formulation is established. The derivation of the problem is coded in Matlab [8] environment for the simulation of perfect point scatterers that emulate different targets. The justification of the imaging algorithm is demonstrated thru the resultant bistatic ISAR images of those targets. At the last section, the work is summarized and the features and the capabilities of bistatic imaging with respect to monostatic case are also discussed.

2. Theory and Formulation

The geometry for the bistatic ISAR imaging problem is illustrated in Fig. 1. The target is assumed to be a point scatterer located at position $(\rho_0, \emptyset_0)$ in polar coordinates. The transmitter *Tx* and recevier *Rx* is at *R* distance away from the origin and their angular positions are specified by two parameters; β and θ as labeled in Fig. 1. β is the bistatic angle between *Tx* and *Rx* and θ is the angle between the bisector of β and the x-axis. It is assumed that the field data is collected in *f* and θ coordinates by keeping *Tx* fixed and changing angle of *Rx* by $\Delta\theta$. This variation of the *Rx* angle will also cause to an identical $\Delta\theta$ change in the monostatic viewing angle θ. Hence for this situation, the angles of *Tx* and *Rx* in polar coordinates can be equivalently assumed to alter with $(\theta - \beta/2)$ and $(\theta + \beta/2)$ respectively.

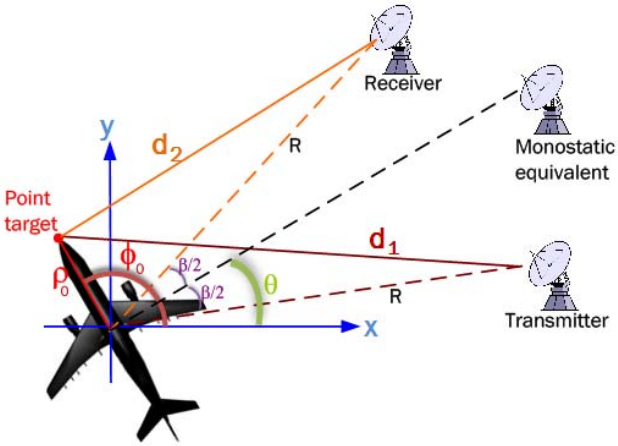

Fig.1. Geometry of the bistatic ISAR imaging.

The distances of *Tx* and *Rx* to the point scatterer can be found from the law of cosines. Assuming that both the transmitter and the receiver are at the far field ($R \gg \rho_0$), then the distance of the point target from the transmitter and the receiver can be calculated by

$$d_1 = R - \rho_0 \cos\left(\emptyset_0 - \theta + \frac{\beta}{2}\right) \quad (1)$$

$$d_2 = R - \rho_0 \cos\left(\emptyset_0 - \theta - \frac{\beta}{2}\right) \quad (2)$$

Then, the scattered electric field from the point on the target can be simply written as the following

$$E^S(f,\theta) = Ae^{-jk(d_1+d_2)} \quad (3)$$

where A is the electromagnetic reflectivity of the point scatterer and $k = \frac{2\pi f}{c}$ is the wavenumber. By substituting the expressions of Eq.(1) and Eq.(2) into Eq.(3), we have

$$E^S(f,\theta) = Ae^{-jk\left(2R-\rho_0\left[\cos\left(\emptyset_0-\theta+\frac{\beta}{2}\right)+\cos\left(\emptyset_0-\theta-\frac{\beta}{2}\right)\right]\right)} \quad (4)$$

By using the cosine expansion, the field can be rewritten as

$$E^S(f,\theta) = Ae^{-jk2R} \cdot e^{jk2\rho_0\cos(\beta/2)\cos(\emptyset_0-\theta)} \quad (5)$$

Let, $E^{SC}(f,\theta) = \mathrm{e}^{\mathrm{jk2R}}E^S(f,\theta)$ represents the field whose phase center is selected as the origin. By applying again the cosine expansion, this phase centered field in Eq.(5) can be obtained as

$$E^{SC}(f,\theta) = Ae^{jk2\rho_0\cos(\beta/2)[\cos\emptyset_0\cos\theta+\sin\emptyset_0\sin\theta]} \quad (6)$$

For the sake of simplicity, if the initial position of the monostatic viewing angle θ_0 is set to 0° then $\theta = \theta_0 + \Delta\theta = \Delta\theta$ and the Eq.(6) becomes more attractive as

$$E^{SC}(f,\theta) = Ae^{jk2\rho_0\cos(\beta/2)[\cos\emptyset_0\cos\Delta\theta+\sin\emptyset_0\sin\Delta\theta]} \quad (7)$$

At this point, we assume that the bandwidth of the transmitted signal is small such that $BW_f \ll f_c$ where f_c is the center frequency and the the variation of the viewing angle $\Delta\theta$ is also small such that $sin\Delta\,\theta \approx \Delta\theta$ and $cos\,\Delta\theta \approx 1$ approximations hold true. By employing these assumptions into Eq.(7), we get

$$E^{SC}(f,\theta) = Ae^{jk2\cos(\beta/2)\rho_0\cos(\emptyset_0)}e^{jk2\cos(\beta/2)\rho_0\sin(\emptyset_0)\Delta\theta} \quad (8)$$

By writing the Cartesian coordinates expression $x_0 = \rho_0\cos(\emptyset_0)$ and $y_0 = \rho_0\cos(\emptyset_0)$ of the point scatterer into Eq.(8), we obtain the following:

$$E^{SC}(f,\theta) = Ae^{jk2\cos(\beta/2)x_0} \cdot e^{jk2\cos(\beta/2)y_0\Delta\theta} \quad (9)$$

If we make a suitable change of variables such that;

$$X = \frac{2f}{c}cos(\beta/2) \text{ and } Y = \frac{2f}{c}\Delta\theta\cos(\beta/2) \quad (10)$$

Then, the Eq.(9) can be rewritten by the new variables together with a new function $E^{SC}(X,Y)$ as follows;

$$E^{SC}(X,Y) = Ae^{j2\pi[Xx_0+Yy_0]} = \int_{-\infty}^{\infty}\int_{-\infty}^{\infty} A\delta(x-x_0,y-y_0)\,e^{j2\pi[xX+yY]}dxdy \quad (11)$$

Looking at Eq.(11), we see that the field E^{SC} is nothing but the spatial Fourier transform of the reflectivity of the scatterer. To obtain the reflectivity image, we can simply take the inverse Fourier transform (IFT) of the scattered data. Prior to this IFT, the data need to be resampled uniformly on the rectangular grid of the $X-Y$ plane. However, this interpolation can be discarded under the small-angle and small-bandwidth approximations. For the general case; therefore, the bistatic ISAR imaging equation finally becomes

$$A\delta(x-x_0,y-y_0) = \int\int E^{SC}(X,Y)e^{-j2\pi[Xx+Yy]}\,dXdY \quad (12)$$

By modeling the target as a sum of finite scattering centers; i.e $\sum_{i=1}^{N} A_i\delta(x-x_i,y-y_i)$, the reflectivies of A_i can be imaged by first phase centering the total scattered field to the target origin and then by applying two-dimensional (2D) IFT. The resolutions in the resulting reflectivity image depend on the bandwidths of the Fourier kernels of Eq.(11). Hence, the range resolution can be readily get as

$$\Delta x = \frac{1}{BW\left(\frac{2f}{c}cos(\beta/2)\right)} = \frac{c}{2BW_f\cos(\beta/2)} \quad (13)$$

where BW denotes the bandwidth. The cross-range resolution can be found as in a similar manner as the following

$$\Delta y = \frac{1}{BW\left(\frac{2f_c}{c}cos(\beta/2)\Delta\theta\right)} = \frac{c}{2f_cBW_{\Delta\theta}\cos(\beta/2)} \quad (14)$$

We see that both range and cross-range resolutions degrade by $cos(\beta/2)$ when compared to the monostatic resolutions. For the range of bistatic angle $\beta \le 90^\circ$, the image distortion caused from this resolution reduction will not be significant. On the other hand, the frequency bandwidth is reduced and shifted to the smaller frequencies comparing with monostatic imaging due to the $cos(\beta/2)$ factor in the imaging process of Eq.(12).

3. Simulation Results

In this section, the simulated images of various point target models for different bistatic configurations will be examined thru the above formulation of the problem. First, an airplane model whose dimension is $10\,m\,x\,10\,m$ in range and cross-range domains is constructed as viewed in Fig. 2. According to the bistatic geometry of Fig.1, the angle θ is initially selected as 0° and the bistatic angle β is selected as 30° for this example. Hence, *Tx* is at -15° and *Rx* is at 15° according to the *x* axis. The frequency is altered within 1 GHz bandwidth from 11 GHz to 12 GHz. The bandwidth of the viewing angle θ is taken as 7° by changing the *Rx* angle with a deviation of -3.5° to 3.5° from its initial position. The image window is chosen as 16 m in both directions which is suitable to cover the whole area occupied by the target. The range and cross-range resolutions are then calculated as 15.53 cm and 10.59 cm, respectively. Comparing with monostatic (15.00 cm range and 10.23 cm cross-range), the resolutions become worse and reduced by a factor of $cos(\beta/2)$. On the other hand, the frequency bandwidth of image reconstruction is better than that of the monostatic and decreased to 0.9659 GHz. After performing the image formulation, the zero-padding procedure is applied to interpolate the image data. To suppress the tails of the point spread response, a Hamming windowing is also employed prior to the IFT operation. The resulted image is shown in Fig.3 (a). As it is seen from the figure, the image quality degradation caused from the bistatic imaging can be regarded as acceptable for this value of $\beta = 30^\circ$.

In order to concern the benefit of the method for a larger bistatic angle, the simulation is then repeated with the same parameters as the previous example and the bistatic angle β is set to 120°. The range and cross range resolutions are calculated

as $30.00\ cm$ and $20.46\ cm$ respectively, whereas the frequency bandwidth is evaluated as $0.5\ GHz$. Comparing these values with the previous example, the main advantage of the method for a larger bistatic angle can be stated as the reduced frequency bandwidth in image reconstruction which is in turn accounted by the poor spatial resolutions. Corresponding ISAR image is shown in Fig.3 (b) and as expected the bistatic geometry distorts the image for a large bistatic angle.

Secondly, the simulation of the airbus model whose implementation with perfect point scatterers is shown in Fig 4. If the monostatic viewing angle θ is set initially to 0° and the bistatic angle β is set to 20° in Fig.1, then *Tx* is at -10° and *Rx* is at 10° with respect to x-axis. Similarly, the bandwidths of the frequency and the viewing angle are selected as identical to the previous simulation. The image window is chosen as $40\ m$ in both directions. The range resolution is $15.23\ cm$ and the cross-range resolution is $10.39\ cm$. The frequency coverage of the image formation extends from $10.833\ GHz$ to $11.81\ GHz$ with a $0.982\ GHz$ bandwidth. As in the previous simulations, after applying the imaging operations of zero-padding, windowing and IFT, the image is obtained as depicted in Fig.5 (a).

At the same simulation, if the bistatic angle β is set to 140°, the range and cross-range resolutions are decreased to $43.86\ cm$ and $29.91\ cm$, respectively and the simulated image is obtained as illustrated in Fig.5(b).

4. Conclusions

In this work, we have provided a practical formulation in forming the bistatic ISAR images of the frequency-domain backscattered data. The well-known direct Fourier inversion theory is rearranged for the bistatic geometry and the imaging characteristics such as frequency-bandwidth and spatial resolutions are investigated throughout this formulation. By comparing with monostatic situation, it has shown that for a bistatic case, the range and cross range resolutions are no longer constant and reduce with the bistatic angle β. Hence, this constitutes an important deficiency of the bistatic imaging. However, for particular values such that $\beta \leq 90^{\circ}$ the resolution degradation has no serious effect on the image quality and can be acceptable for most applications. On the other hand, the descent in the frequency bandwidth of imaging process can be regarded as the certain success of the bistatic imaging over the monostatic one. Besides, the main improvement of bistatic reasoning is the capability of providing different observation angles of the target. These benefits and drawbacks of bistatic imaging have also been visualized and validated by the simulated images of various point target models.

For the continuation of this research work, the algorithm will be tested by real electromagnetic simulators that can provide reliable simulations of large and complex bodies at high frequencies.

5. References

[1] P. Tait, "Introduction to radar target recognition", IET, UK, 2006.

[2] D. L. Mensa, "High resolution radar cross-section imaging", Artech House, Norwood, MA, 1991.

[3] M. P. Simon, M. J. Schuh and A. C. Woo, "Bistatic ISAR images from a time-domain code", *IEEE Antennas and Propagation Magazine,* vol. 37, no. 5, pp. 25-32, 1995.

[4] M. Martorella, J. Palmer, J. Homer, B. Littleton and I. D .Longstaff, "On bistatic inverse synthetic aperture radar", *IEEE Transactions on Aerospace and Electronic Systems,* vol. 43, no. 3, pp. 1125-1134, 2007.

[5] Z. Zhu, Y. Zhang and Z. Tang , "Bistatic inverse synthetic aperture radar imaging", *IEEE International Radar Conference,* Crystal Gateway Marriott Arlington, VA, 2005*,* pp. 354- 358.

[6] B. Yılmaz and C. Ozdemir, "Nümerik yöntemlerle saçılan alan hesabı, 3-B ters yapay açıklı radar görüntülerinin elde edilmesi ve saçılma merkezleri analizi", *4. Savunma Teknolojileri Kongresi (SAVTEK 2008)*, Ankara, 2008, pp. 259-267.

[7] B. Yılmaz and C. Ozdemir, "Ters yapay açıklıklı radar görüntülerindeki saçılma merkezi analizi yardımıyla büyük ve karmaşık platformların radar soğurucu malzeme ile kaplanarak RKA'larının azaltılması", *URSI-TÜRKİYE'2008 Bilimsel Kongresi*, Antalya, 2008.

[8] MATLAB R2007a, *The MathWorks Inc.*, 2007.

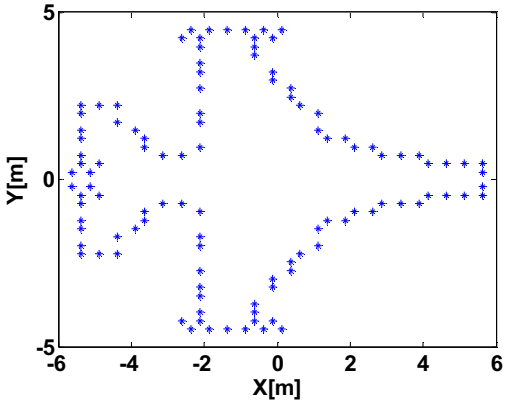

Fig2. The geometry of an airplane target.

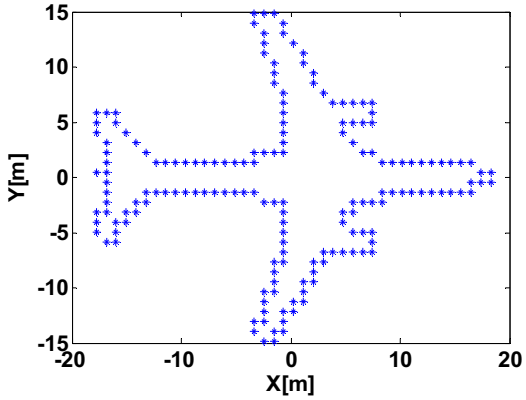

Fig4. The geometry of an airbus target.

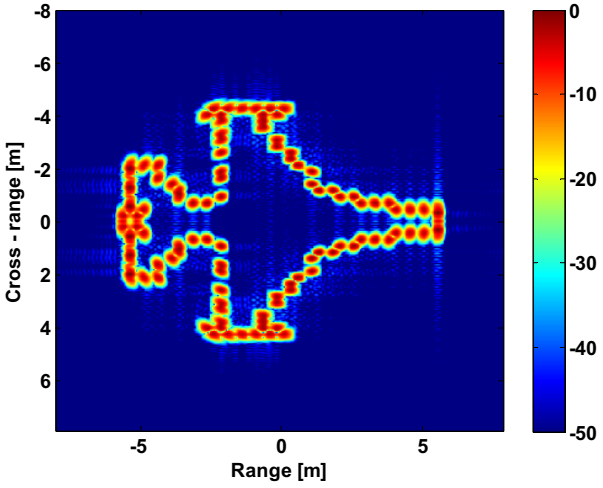

(a)

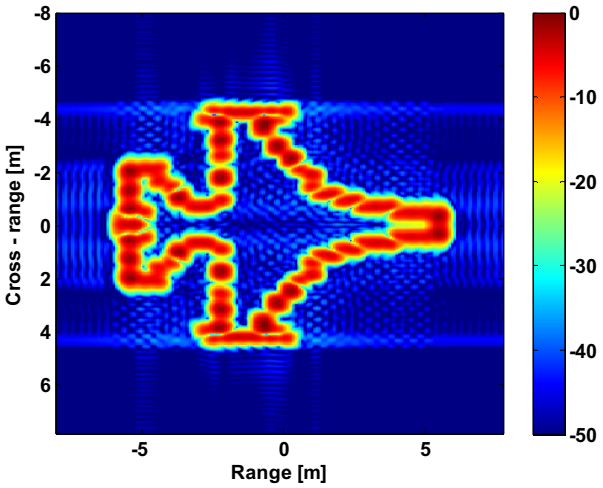

(b)

Fig.3. The simulated image of an airplane target for the bistatic angle (a) $\beta = 30℃$ and (b) $\beta = 120℃$.

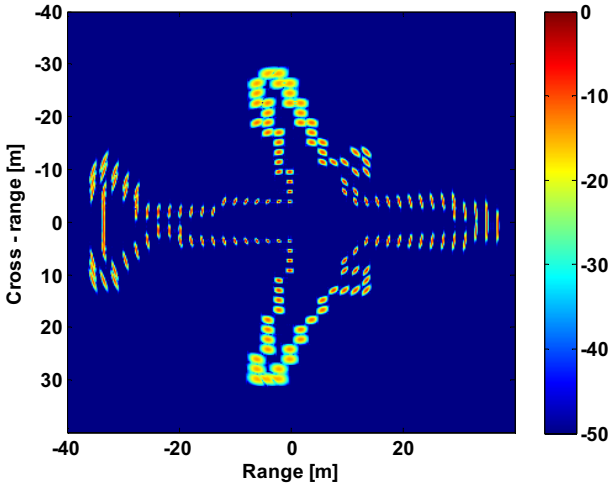

(a)

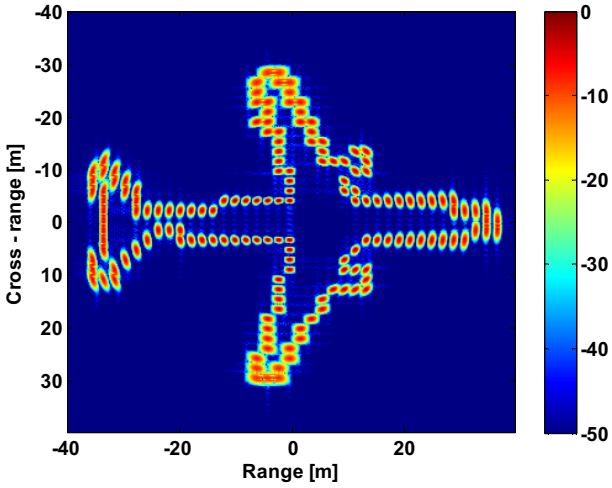

(b)

Fig.5. The simulated image of an airbus target for the bistatic angle (a) $\beta = 20℃$ and (b) $\beta = 140℃$.